

Water Resources Research

TECHNICAL REPORTS: METHODS

10.1029/2020WR027257

Key Points:

- A novel automatic instrument is developed for high-frequency intertidal bed level dynamics observation
- Data transmission function enables building automatic bed level observation networks to support coastal research and management
- Machine learning applications reveal that the presence of vegetation plays a key role in mangrove biogeomorphic processes

Supporting Information:

- Supporting Information S1

Correspondence to:

Y. Peng and P. Zheng,
 pyish@mail.sysu.edu.cn;
 zhengpeng@ouc.edu.cn

Citation:

Hu, Z., Zhou, J., Wang, C., Wang, H., He, Z., Peng, Y., et al. (2020). A novel instrument for bed dynamics observation supports machine learning applications in mangrove biogeomorphic processes. *Water Resources Research*, 56, e2020WR027257. <https://doi.org/10.1029/2020WR027257>

Received 4 FEB 2020






Accepted 12 JUN 2020

Accepted article online 14 JUN 2020

©2020. The Authors.

This is an open access article under the terms of the Creative Commons Attribution-NonCommercial License, which permits use, distribution and reproduction in any medium, provided the original work is properly cited and is not used for commercial purposes.

A Novel Instrument for Bed Dynamics Observation Supports Machine Learning Applications in Mangrove Biogeomorphic Processes

Z. Hu^{1,2} , J. Zhou¹, C. Wang³, H. Wang¹, Z. He¹, Y. Peng^{2,4} , P. Zheng⁵ , F. Cozzoli^{6,7} , and T. J. Bouma⁸ 

¹Guangdong Provincial Key Laboratory of Marine Resources and Coastal Engineering, and School of Marine Science, Sun Yat-sen University, Guangzhou, China, ²Southern Marine Science and Engineering Guangdong Laboratory, Zhuhai, China, ³Satellite Application Center for Ecology and Environment, Ministry of Ecology and Environment, and State Environmental Protection Key Laboratory of Satellite Remote Sensing, Beijing, China, ⁴School of Environmental Science and Engineering, Sun Yat-Sen University, Guangzhou, China, ⁵College of Oceanic and Atmospheric Sciences, Ocean University of China, Qingdao, China, ⁶Dipartimento di Scienze e Tecnologie Biologiche ed Ambientali, University of the Salento, Lecce, Italy, ⁷Research Institute on Terrestrial Ecosystems (IRET) - National Research Council of Italy (CNR), Monterotondo Scalo, Italy, ⁸Department of Estuarine and Delta Systems, Royal Netherlands Institute of Sea Research (NIOZ) and Utrecht University, Yerseke, Netherlands

Abstract Short-term bed level changes play a critical role in long-term coastal wetland dynamics. High-frequency observation techniques are crucial for better understanding of intertidal biogeomorphic evolution. Here, we introduce an innovative instrument for bed level dynamics observation, that is, LSED-sensor (Laser based Surface Elevation Dynamics sensor). The LSED-sensors inherit the merits of the previously introduced optical SED sensors as it enables continuous high-frequency monitoring with relatively low cost of labor and acquisition. As an iteration of the optical SED-sensors, the LSED-sensors avoid touching the measuring object (i.e., bed surface), and they do not rely on daylight by adapting laser-ranging technique. Furthermore, the new LSED-sensors are equipped with a real-time data transmission function, enabling automatic observation networks covering multiple (remote) sites. During a 22-day field survey in a mangrove wetland, good agreement ($R^2 = 0.7$) has been obtained between the automatic LSED-sensor measurement and an accurate ground-truth measurement method, that is, Sedimentation Erosion Bars. The obtained LSED-sensor data were subsequently used to develop machine learning predictors, which revealed the effect of vegetation is a main driver in the accumulative and daily bed level changes. We expect that the LSED-sensors can further support machine learning applications to extract new knowledge on coastal biogeomorphic processes.

1. Introduction

Monitoring bed level changes is of key importance in assessing coastal wetland resilience to climate changes stresses (Horstman et al., 2015; Leonardi et al., 2018; van Bijsterveldt et al., 2020; Yang et al., 2008). Recent lab and field experiments have revealed that short-term (daily) bed level dynamics plays a critical role in long-term coastal wetland dynamics by affecting the seedling establishment process and the onset of vegetation later retreat (Balke, et al., 2013; Bouma et al., 2016; Cao et al., 2018). Therefore, data sets with high temporal and spatial resolutions are needed for improved understanding and prediction of intertidal biogeomorphic evaluations.

Conventionally, intertidal bed level changes are monitored by manual surveys. These manual methods are generally precise and low cost, but not suitable for high-frequency (e.g., daily) monitoring, due to excessive labor involved (Hu et al., 2015, and see Table A1 in Appendix A). Automated instruments have been developed and improved over the years to achieve the high-frequency bed level monitoring. A recent development in the automated bed-level monitoring technique is the invention of a low-cost precise instrument called Surface Elevation Dynamics sensor (SED-sensor) (Hu, Lenting, et al., 2015). It detects bed surface position by an array of optical cells inserted into sediment bed. Thus, these sensors are referred as optical SED-sensors hereafter. The optical SED-sensors are proven to be useful in providing high-resolution intertidal bed level dynamics data (Baptist et al., 2019; Belliard et al., 2019; Hu et al., 2017; Willemsen

et al., 2018) and testing dynamic equilibrium theory of tidal flat morphology (Hu et al., 2015, 2018). However, there are two main shortcomings of this sensor. First, it directly touches the monitoring object (i.e., the bed surface), which may influence the measurement. Second, as the sensors depend on daylight to operate, their measuring windows are restricted to low tides during daytime. Bed level cannot be monitored during nighttime.

To overcome these limitations, we designed a new instrument based on laser-ranging technique for automatic bed level change observation: Laser-based Surface Elevation Dynamic sensor (LSED-sensor). It detects the bed elevation using laser ranging method to avoid touching the measuring bed surface and the dependence of daylight. Similar to the optical SED-sensor, it can provide long-term high-frequency monitoring at a relatively low cost of labor and acquisition (Table A1). The price of a LSED-sensor (4,000 USD) is only one fifth of the Acoustic instruments. Additionally, we equip the sensor with a data transmission function via 4G mobile networks to achieve real-time monitoring and prompt data retrieve.

The LSED-sensors can provide accurate and high-frequency bed level dynamic data to support the development of machine learning applications. Biogeomorphic processes in intertidal wetlands are typically nonlinear and influenced by a number of factors, for example, hydrodynamic forcing, sediment property, and vegetation cover (Friedrichs, 2011). Accurate prediction of these processes is generally challenging for process-based morphodynamic models. With recent development in the algorithms and computation power, machine learning techniques have shown promising potentials in generating insights and quantitative relations in intertidal morphodynamic processes (see Goldstein et al., 2019, for a recent review). Compared to process-based models (Maan et al., 2015; Zhou et al., 2014, 2016), the predictivity of machine learning applications largely depends on the quality and frequency of the data sets.

The main goal of this study is to introduce the new LSED-sensors for bed level measurement and test their performance in a mangrove wetland with multiple stations. The observed spatiotemporal bed dynamics pattern in the mangrove wetland is interpreted in relation with the local biophysical settings, for example, tidal level, wave, and vegetation cover. Furthermore, we demonstrate how the obtained bed level data can be used in machine learning applications to identify the main factors influencing bed level changes.

2. Materials and Methods

2.1. Design of the New LSED-Sensor

The LSED-sensor is a standalone instrument aimed to accurately measure bed level change (Figure 1). The measuring and supporting components of the sensor (e.g., data logging and battery) are all enclosed in a transparent organic glass tube, which is 5 mm thick to ensure durability. When in use, it is installed on a stainless steel rack. The measuring part of the sensor contains four downward-looking laser probes, which are placed 10 cm apart. The probes are installed about 1 m above the bed to measure the distance to the bed surface (Z). The laser beams from the probes should be perpendicular to the bed, which is ensured by using a leveling bubble on the mainboard (Figure 1b). In one measurement, each probe sends out and receives laser signal 10 times. The sensor subsequently records the mean value of these 10 readings as one measurement of each probe. The number of readings is a balance between accuracy and battery consumption. To avoid the possible bias caused by small sand ripples, the mean Z of four probes can be computed to reflect averaged bed level position.

As the laser beams are refracted by water on the bed, we only analyze the data when the water is drained during low tide. Therefore, the effective measuring interval of the sensor is one tidal cycle. Water content in the surface sediment may also lead to refraction of laser beams and affect the measurements. Thus, a laboratory experiment was conducted prior to the field deployment, which showed that the accuracy of the sensor was not affected by sediment water content as long as there was no lingering water on the sediment surface (Appendix B).

Monitoring configuration of the sensor can be done by using a LED touch panel (Figure 1c) or by smart phones via Bluetooth. The latter option allows us to reconfigure the sensor in field without disturbing the setup. The LED touch panel also displays status of the sensor including date, Z , temperature, humidity, and battery usage. These data are logged locally in a micro-SD card and on a cloud server via 4G mobile networks at user-defined intervals. In such way, we reduce the risk of losing data and also facilitate building

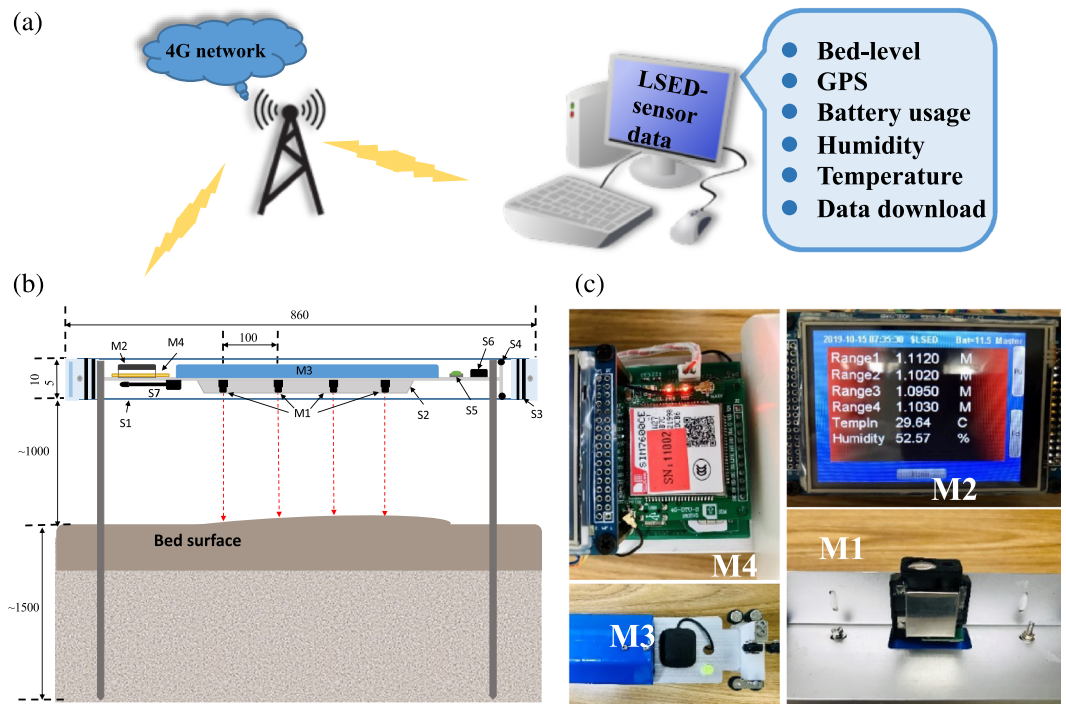


Figure 1. Design and photos of the LSED-sensor. (a) Real-time data transmission function of the LSED-sensor via 4G mobile network. (b) Design of the LSED-sensors with measurement components (M) and supporting components (S). The indicated dimensions are in mm (not to scale). M1 is laser probes; M2 is a LED screen; M3 is battery; M4 is a circuit board; S1 is a transparent organic glass tube; S2 is an aluminum alloy plate; S3 is silicone rings; S4 is fixed wheels; S5 is a leveling bubble; S6 is a GPS module; and S7 is a Bluetooth antenna. (c) Detailed photos of M1–M4.

automatic observation networks across multiple sites. To allow long-term measurements, the sensor is equipped with high-capacity rechargeable batteries. The estimated measuring duration is longer than 6 months if the measuring frequency is once per hour and data communication frequency is once per day. More detailed information of the sensor, for example, bill of materials, sources for purchasing the hardware, and wiring diagram, can be found in the supporting information.

2.2. Field Experimental Setup

In 10–29 December 2018, we deployed three LSED sensors in a mangrove wetland on the Hailing island in the south of China (Figures 2a and 2b). The monitored tidal flat is a mesotidal system with irregular semi-diurnal tide. The mean tidal range is 2.5 m. The maximum tide range can reach 3 m, and minimum tide range is 0.5 m. To test the impact of vegetation existence on bed level dynamics, the sensors were deployed on a transect with three stations, with different vegetation coverage, that is, Station M (Mangrove forest), Station P (Pioneer zone), and Station B (Bare tidal flat). The monitoring transect was approximately 100 m long (Figure 2c). The bathymetry of the transect was obtained by a RTK survey. The elevations of Stations B, P, and M relative to the mean sea level are 0.19, 0.29, and 0.32 m, respectively. At our study site, the mature mangrove area is occupied by dense tall (2–3 m) *Avicennia marina* trees, whereas the pioneer zone is occupied by sparse seedlings. The boundaries between mangrove forest, pioneer mangrove, and the bare flat areas are distinct. The bed surface sediment of our site consists of fine sand. The median grain size (D_{50}) is 0.27 mm at Station B, and it reduced to 0.08 mm at Station M.

The measurement interval of LSED-sensors was set as 30 min in our field survey. We noted Z at the start of the measurement as $Z(t_0)$. The accumulative bed level change is then calculated by $Z_A = Z(t_i) - Z(t_0)$, where $Z(t_i)$ is the bed level position at tide cycle t_i . The tidally bed-level change Z_{tide} can be calculated as: $Z_{tide} = Z(t_{i+1}) - Z(t_i)$. To test the performance of LSED-sensors, we compared the accumulative bed level change (Z_A) obtained by the LSED-sensor to a precise manual method, that is, Sediment Erosion Bar (SEB). At each station, the SEB measurements were taken daily during low tide in daytime. To facilitate

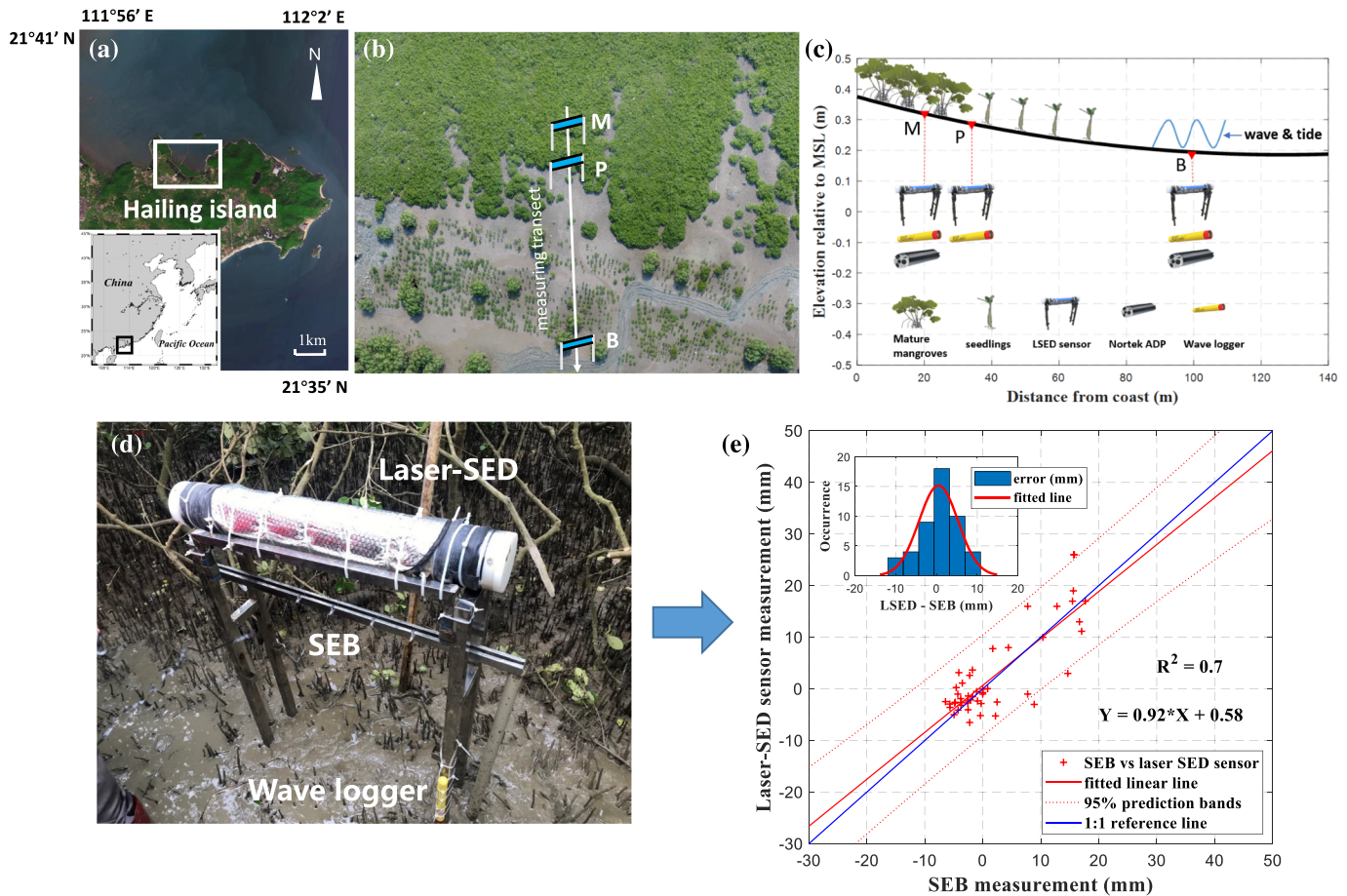


Figure 2. (a) Study site at the northeast site of the Hailing island, China. (b) Transect with three measuring stations, where M is the Mature mangrove site, P is the Pioneer zone site, and B is the Bare flat site. (c) An overview of instruments deployments and the bathymetry of the measuring transect. (d) LSED-sensor and Sediment Erosion Bar (SEB) in field. (e) Comparison of accumulative bed level change (Z_A) obtained by the LSED-sensor and the manual SEB measurement ($R^2 = 0.7$). Positive and negative values represent sedimentation and erosion, respectively. The inset shows the error distribution histogram.

the comparison, Z_A monitored by the LSED-sensors was resampled from tidally interval to daily interval, whereas for other analysis Z_A was kept its original tidally interval.

Overall, the Z_A monitored by the LSED-sensors at our field site show a good agreement with that obtained by the SEB ($R^2 = 0.7$; Figure 2e). Based the data from these two methods, a fitted regression function can be derived as $Y = 0.92 \cdot X + 0.58$. The slope of the regression function is fairly close to 1, and the intercept is small. Additionally, almost all of the data points are within the 95% prediction bands. They were calculated as $Y \pm \text{DELTA}$, where Y is the prediction value at X and DELTA is an estimate of the standard error of the prediction with 95% confidence level. If we set the precise SEB measurement as a benchmark, the accuracy of the LSED-sensor can be defined as the mean absolute error between the LSED-sensor and SEB measurements, which is 3.5 mm.

Nortek ADPs (Acoustic Doppler Profiler) were used to measure current velocity profiles at Stations M and B, as these two sites represent the landward and seaward limits of our transect. ADP profilers were placed in holes in the bed leaving the measuring head upward looking. The measuring interval of the velocity profile is 10 min. As there is no velocity measurement at Station P, the long-shore velocity (the main velocity component) there is calculated based on the model of Le Hir et al. (2000) using data from Station B: The ratio between the velocities at these two sites is proportional to the square of the water depth ratio. At each station, significant wave heights (H_s), wave periods, and water depth (h) were measured using a pressure sensors (RBR solo³), tied to the rack of LSED-sensor. The measuring tips of the sensor were 5 cm above the bed. These sensors measured wave parameters and water depth at a 10-min interval. In each measurement, a

Table 1
Input and Output Variables in MLPs

Predictors	Case	Input				Output		
		τ_{max}	Water depth (h)	Vegetation density (VD)	Station	Z_A	Z_{tide}	Station
MPL1	1	●	●	●	B-P-M	●	○	B-P-M
	2	○	●	●	B-P-M	●	○	B-P-M
	3	●	○	●	B-P-M	●	○	B-P-M
	4	●	●	○	B-P-M	●	○	B-P-M
MPL2	5	●	●	●	B-P-M	○	●	B-P-M
	6	○	●	●	B-P-M	○	●	B-P-M
	7	●	○	●	B-P-M	○	●	B-P-M
	8	●	●	○	B-P-M	○	●	B-P-M
MPL3	9	●	●	●	B	○	○	B
	10	●	●	●	B	●	○	P
	11	●	●	●	B	●	○	M

Note. Solid and open circles denote included and excluded variables, respectively. B-P-M means the input/output variables are from/for all the three stations.

total of 4,096 bursts of pressure were obtained at 8-Hz frequency. Bed shear stresses induced by waves (τ_w), currents (τ_c), and the mean and maximum bed shear stresses with combined wave and current (i.e., τ_{mean} and τ_{max}) were quantified following Soulsby (1995).

2.3. Developing Machine Learning Predictors Based on LSED-Sensor Data

To demonstrate how the LSED-sensor data can be used in machine learning and reveal the driving factors of the observed bed level dynamics, we built three Machine Learning Predictors (i.e., MLP1–MLP3) using three-layer feed forward Artificial Neural Networks (Yoo et al., 2013, and see Appendix C for the algorithm). These three predictors were trained with biophysical data (e.g., water depth, H_s , τ_{max} , D_{50} , and vegetation density [VD]) to predict the observed accumulative or tidally bed level changes (Z_A and Z_{tide}). An overview of the input and output variables of these predictors is given in Table 1. R^2 values between the prediction and observation were used to evaluate the performance of the predictors.

Nine variables were considered as potential inputs of the MLPs: h (water depth), H_s , τ_w , τ_c , τ_{mean} , τ_{max} , D_{50} , U_{bot} (near bottom current velocity), and VD. We used the 90th percentile τ_{max} , H_s , U_{bot} , and h in a tidal cycle to be the tidally representative value. The 90th percentile value accounts for both the characteristic magnitude of each factor and the fraction of time that factor is effective (Friedrichs, 2011; Friedrichs & Wright, 2004). To discretize the spatial distribution with dense, sparse, and no vegetation, the VD is assigned as 1, 0.5, and 0 for Stations M, P, and B, respectively. Prior to the MLP training, a pairwise correlation analysis was performed for all the input variables to obtain the groups of independent variables (Appendix C). We selected the groups of variables, in which the absolute Pearson's coefficient between each two variables is lower than 0.5, as inputs in the machine learning procedure (Yoo et al., 2013).

MLP1 and MLP2 were trained with data from all the three stations (Table 1). To identify the most critical variable influencing Z_A and Z_{tide} , we tested cases that exclude one of the input variables (Cases 2–4 and 6–8; Coco et al., 2011). Similar to the MLP1, the MLP3 was built to predict Z_A , but it was trained only with the data from the most seaward station (i.e., Station B). The bed level dynamics and hydrodynamics at this station show much larger variations comparing to the other two stations (Figure 3). It is then interesting to test if the MLP3 trained at the station with greater variations can also be applied to other stations with smaller bed level dynamics.

3. Results

3.1. Spatiotemporal Bed Level Dynamics Measured by the LSED-Sensors

The high-frequency LSED-sensor data have shown that the Z_A in the mature mangrove is very different from that on the bare tidal flat (Figure 3d vs. 3l); the p value between these two data sets is 0.00 in a t test. Z_A at Station B (bare flat station) experienced an accretion-erosion cycle: accretion in the neap tide and the erosion in the spring tide. However, bed level at Station M (mature mangrove station) is much more stable, with Z_A

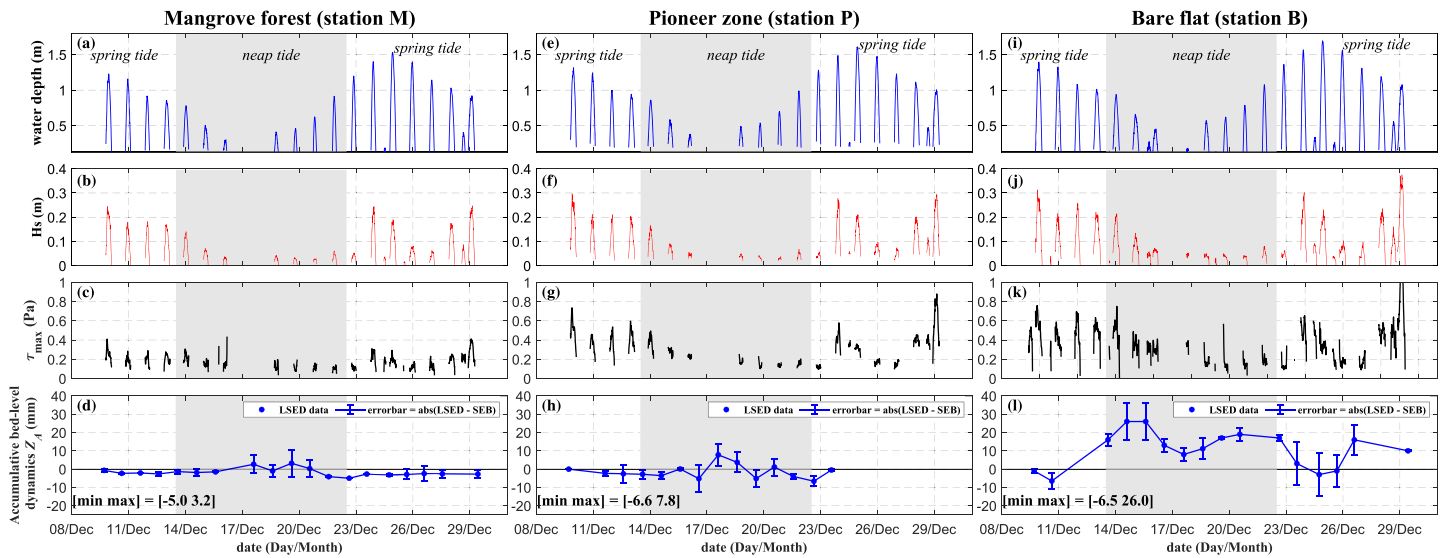


Figure 3. Time series of water depth, significant wave height (H_s), bottom current velocity (U_{bot}), and accumulative bed level changes (Z_A) over each tide at Stations M, P, and B. Error bars in (d), (h), and (l) indicate the absolute difference between the LSED-sensor and the SEB measurement at Station P stops after 24 December due to sensor leakage.

within 5 mm. The magnitude of bed level dynamics at Station P is in between the other two stations (Figure 3h). Significant wave height (H_s) and τ_{max} are reduced from the bare flat to the mangrove (Figure 3). The temporal variation of these two variables seems to be regulated by the tidal level. In addition to the temporal variations shown in Figure 3, spatial variations of Z_{tide} magnitude and bed shear stresses are included in Appendix D.

3.2. Machine Learning Applications Based on LSED-Sensor Data

To reveal the main drivers of the measured bed level dynamics, two machine learning predictors, that is, MLP1 and MLP2, were built based on the observed accumulative and tidally bed level changes (Z_A and Z_{tide}), respectively. In MLPs, three parameters were listed as inputs, that is, τ_{max} , h (water depth), and VD. These parameters were chosen as they do not correlate with each other (Appendix C), and they can result in highest coefficient of determination (R^2) in MLPs.

When all the three input parameters are included (Case 1), an excellent agreement between the measured Z_A and the prediction of MLP1 can be obtained ($R^2 = 0.87$) (Figure 4a). In Cases 2–4, as one out of three inputs was excluded, the R^2 value is substantially reduced. Notably, when VD is excluded from the prediction in Case 4, the R^2 value reaches the minimum value as 0.27. In the assessment of Z_{tide} in MLP2 (Figures 4e–4h), the highest R^2 value is 0.77 in Case 5 when all the three parameters are considered. In Cases 6–8, the R^2 values decrease as one of the input parameters is excluded. Particularly, when the VD (Case 8) is excluded, the drop of the R^2 value is the most significant.

MLP3 was only trained with Z_A from the most seaward Station B (Figure 5). Yet we apply it to predict the accumulative bed level dynamics at all three stations to provide practical implications for using machine learning technique in assessing intertidal morphodynamics. We show that the model can well reproduce the time series of Z_A at Station B. However, the performance of MLP3 at the other two stations (Stations P and M) is poor (Figures 5b and 5c). The implication of the MLP3 performance is discussed in the following section.

4. Discussion and Conclusions

4.1. A Novel Sensor for Automatic Bed Level Measurements

The good agreement between the precise SEB and LSED-sensor measurement shows that the LSED-sensor is a reliable instrument for automatic high-frequency bed dynamics monitoring. The accuracy of the

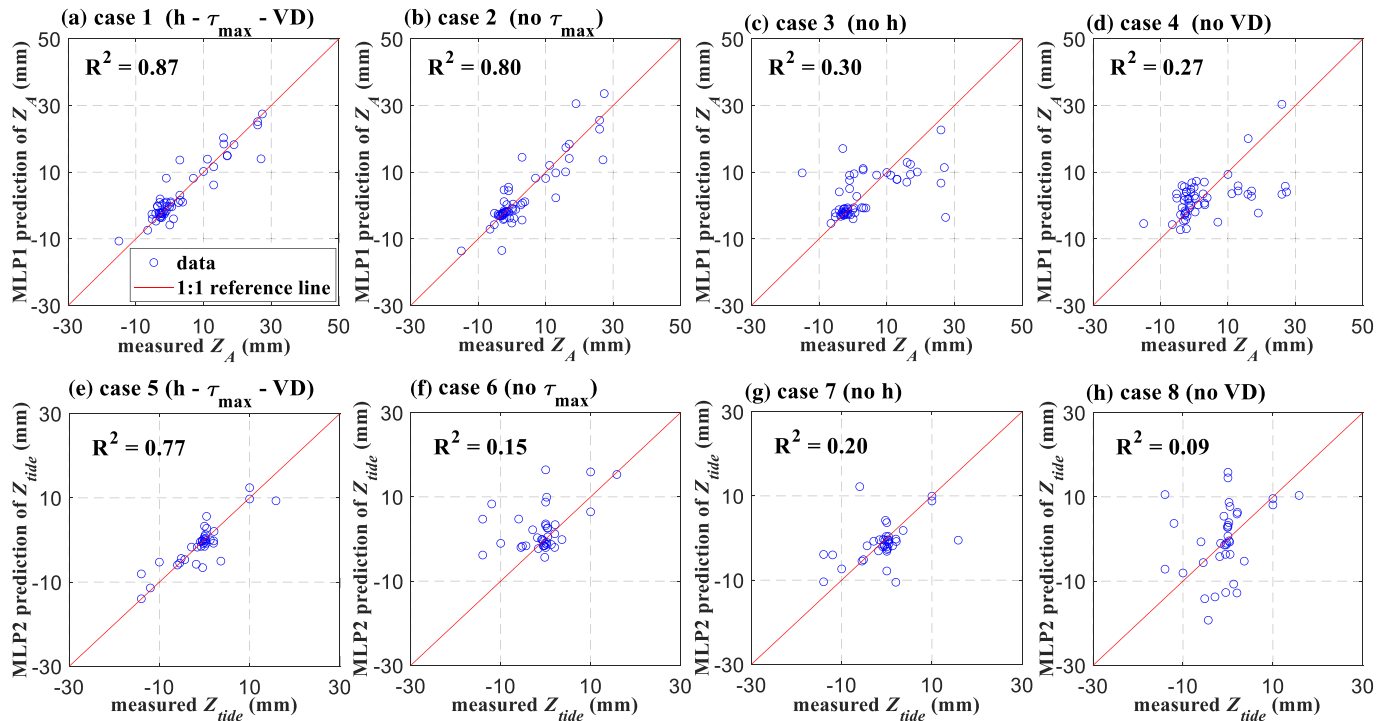


Figure 4. Measured accumulative bed level dynamics (Z_A) versus MLP1 prediction (a–d) and measured tidally bed level dynamics (Z_{tide}) versus MLP2 prediction (e–h). (a) Case 1 is the case run with all the three inputs: τ_{max} , h (water depth), and VD (vegetation density), whereas (b) Case 2 excludes τ_{max} , (c) Case 3 excludes h , and (d) Case 4 excludes VD. (e) Case 5 is the case run with all the three inputs, whereas (f) Case 6 excludes τ_{max} , (g) Case 7 excludes h , and (h) Case 8 excludes VD.

LSED-sensor (3.5 mm) is comparable to that of SED-sensor (5.0 mm; Hu, Lenting, et al., 2015). Similar to the optical SED-sensors, the LSED-sensor is relatively low cost and can reduced the labor in conducting high-frequency bed level measurements (see also Table A1).

In previous studies, the optical SED-sensors have been applied to provide high-frequency bed level change data that lead to advancement in understanding tidal flat dynamic equilibrium (Hu et al., 2018; Hu, Wang, et al., 2015) and the marsh edge lateral dynamics (Willemsen et al., 2018). Comparing to the optical SED-sensors, the main advantages of the new LSED-sensors are as follows: (1) They monitor the bed level by laser ranging technology; hence, they avoid touching the bed surface during measurements; (2) the LSED-sensors do not rely on daylight, so they can still operate in nighttime, which increases the number of measuring windows; (3) the equipped real-time data transmission and inspection functions facilitate building automatic observation networks across multiple (remote) sites via 4G cellular signals. These observation networks can be useful in conducting long-term (months to years) real-time bed level monitoring programs at different sites, which can be useful in selecting restoration sites (Lee et al., 2019; Lee & Khim, 2017) and capture infrequent storm events (Hu et al., 2017; Yang et al., 2008).

The LSED-sensors still have some limitations. First, the deployment of the LSED-sensors is not as convenient as the optical SED-sensors, and unstable installation of sensor may lead to error in the measurement. The sensors need to be deployed on a rack that needs to be installed in advance. In the current study, it takes about 1.5 hr to install one rack. The end tip of rack was driven into the soil with force until refusal (~1.5 m deep into the bed in our case). The difference between the LSED-sensor and the SEB measurements is likely induced by the unstable installation of the sensor racks, as the mean absolute error can be sufficiently reduced in laboratories when the sensor is firmly installed (e.g., Figure B1). In future deployments, the racks of the sensor can be inserted deeper into the sediment with machinery (e.g., handheld drilling machine) to provide sturdier support from the base and reduced the error. Second, the LSED-sensors cannot measure the bed level when there is water on the bed surface due to laser beam refraction. To prevent the influence of lingering water in our field observation, the LSED-sensors were deployed together with

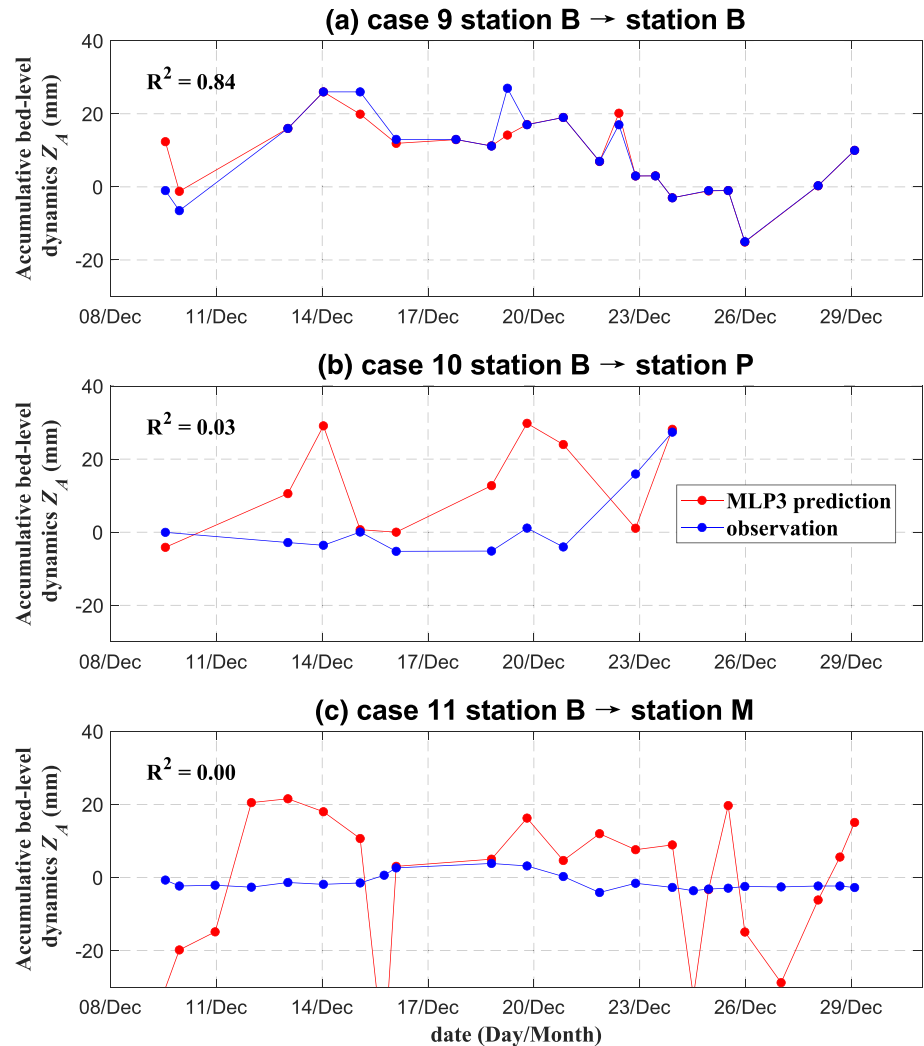


Figure 5. Comparison between the measured accumulative bed level dynamics (Z_A) and the MLP3 predictions for three stations. MLP3 was developed only using the data from Station B. (a) Case 9 uses MLP3 to predict Z_A at Station B; (b) Case 10 uses MLP3 to predict Z_A at Station P; and (c) Case 11 uses MLP3 to predict Z_A at Station M.

pressure sensors to record the tide levels. We assumed that water is completely drained during low tide. In future, we plan to install an automatic camera in the sensor, which will take photos of the bed simultaneously with each bed level measurement (e.g., every 30 min). These photos will be analyzed via machine learning to detect if there is water or litter on the bed. In such way, the imperfect bed level measurements can be automatically removed.

4.2. Machine Learning Applications in Biogeomorphic Systems

Our results demonstrate that the LSED-sensor is a well-suited instrument to support machine learning applications in coastal biogeomorphic research. The developed MLPs can accurately reproduced the accumulative as well as tidally bed level changes. Although theoretical and process-based models have continuously shed lights on coastal morphodynamic evolutions (D'Alpaos et al., 2016; Schuerch et al., 2018; Schwarz et al., 2018; Zhou et al., 2017), our ability to accurately model bed level dynamics, especially the short-term (e.g., tidally) dynamics, is still limited. Machine learning techniques provide excellent tools to extract insight and quantitative relationships from multidimensional nonlinear data sets (e.g., Goldstein & Coco, 2014; Tinoco et al., 2015). Our MLP results show that the effect of vegetation is the most important factor in explaining the spatial difference of bed level dynamics among these three sites compared to

other variables (Cases 4 and 8). Similarly, a previous machine learning study revealed that sea grass cover was the main driver in observed temporal bed level dynamics (Coco et al., 2011). These results are in agreement with previous studies that coastal vegetation has a strong influence on spatiotemporal bed dynamics, which creates a stable sediment dynamic environment favoring their own long-term growth (e.g., Ladd et al., 2019; Liu & Nepf, 2016; Schuerch et al., 2018; Truong et al., 2019).

The modeling results of MLP3 indicated that class imbalance is important in selecting training data. If a few sets of data from Stations P and M were included for training of MLP3, the performance may be improved (Case 1). In addition, suspended sediment concentration is not measured in the current study due to instrument shortage, but it is a relevant input variable influencing bed dynamics (Dai et al., 2016, 2018). Thus, a general machine learning predictor for intertidal morphodynamics would benefit from (1) data sets of large spatiotemporal coverage to eliminate class imbalance, (2) comprehensive data sets including all relevant variables including also biological processes (e.g., Cozzoli et al., 2019), and (3) adoption of more advanced machine learning techniques such as Recurrent Neural networks and Long Short-Term Memory (LSTM) networks (Kratzert et al., 2018; Pape et al., 2007, 2010). These suggestions may provide a way forward for machine learning applications in analyzing intertidal bed level dynamics data. The combination of the machine learning approach and the high-frequency bed level observation system is expected to generate new insights of coastal biogeomorphic processes in future studies.

Appendix A: A Review of Manual and Autonomous Methods for Intertidal Bed Level Dynamics Observation

Table A1
List of Manual and Autonomous Methods for Intertidal Bed Level Dynamics Observation

Category	Method	References	Vertical resolution (mm)	Typical measurement interval	Touching the measuring bed	Working range	Working Condition	Price range (U.S. dollar)
Manual methods	SET/SEB	Cahoon et al., 2002; Gong et al., 2017; Rogers et al., 2014	0.5–1.5	Weeks to months	No	Point	Dry	<100
	Triple-rod method	Zhu et al., 2014	~5–10	Weeks to months	No	Point	Dry/wet	<50
	Erosion pins	Gabet, 1998; Willemsen et al., 2018	~10	Weeks to months	Yes	Point	Dry	<5
	Buried plate	Zhu et al., 2017	~20	Weeks to months	Yes	Point	Dry	<20
	RTK-GPS	Bearman et al., 2010; Zhao et al., 2017	~10–20	Weeks to years	No	Point	Dry	4,000–20,000
	LiDAR	Ge et al., 2017; Nagihara et al., 2004	~6	Weeks to years	No	0.3 km ²	Dry	~100,000
	Photogrammetry/SfM (UAV)	Fonstad et al., 2013; Zhu et al., 2019	~50	Weeks to years	No	0.1–1 km ²	Dry and weak wind	2,000–20,000
Autonomous methods	PEEP	Lawler, 1991, 2008	~2.3	Days	Yes	Point	Dry/wet	~2,000
	Acoustic sensors	(Andersen et al., 2006; Jestin et al., 1998; Shi et al., 2019; Yu et al., 2017; Zhu et al., 2014)	~1	Minutes	No	Point	Wet	20,000–40,000
	Optical SED-sensor	Baptist et al., 2019; Hu, Lenting, et al., 2015; Willemsen et al., 2018	2	up to 1 s	Yes	Point	Dry	~1,500
	LSED-sensor	This paper	1	up to 1 s	No	Point	Dry	~4,000

Note. The “dry” condition means when the tidal flat is drained, while the “wet” condition means when the tidal flat is inundated.

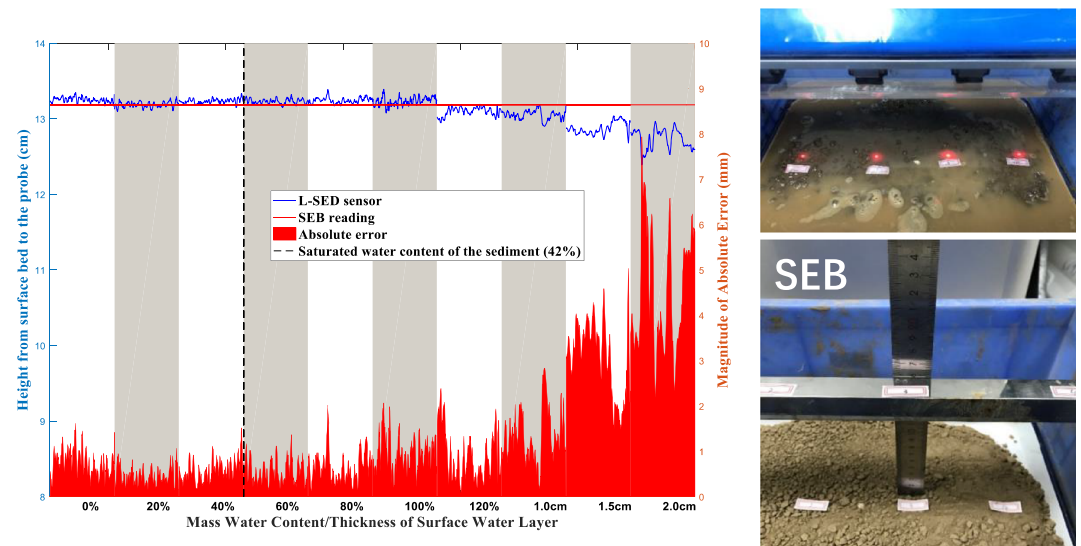


Figure B1. Laboratory experiment results of LSED-sensor versus SEB with different sediment water content.

Appendix B: Laboratory Experiment of LSED-Sensor Measurement With Wet Surface Sediment

Water content in the surface sediment can lead to laser beam refraction and influence the LSED-sensor measurements. Thus, prior we used the LSED-sensor in the field, a laboratory experiment was conducted to test its accuracy when the bed surface sediment contains water. Ten different water mass contents were tested in this experiment. Water mass content is defined as

$$\omega = \frac{M_{water}}{M_{sed}} \times 100\%, \quad (B1)$$

where M_{water} denotes mass of water and M_{sed} denotes mass of sediment that is absolute dry. The experiment starts with sediment of zero water content, which has been dried in an oven at 120°C for 24 hr. We gradually increased the mass water content to the 100%, while the sediment saturation limit is 42%. When the mass water content reached up to 120%, there was a thin layer of water on the surface bed. We subsequently used the thickness of water layer as a measure for the amount of water exists on sediment surface.

We measured the height from sediment bed to the probe with both LSED-sensor and a simplified SEB (Figure B1). During each water content, the LSED-sensor measured the bed level every 3 s for 15 min. Absolute errors between the SEB and LSED-sensor were calculated by the formula $e = Z_{LSED} - Z_{SEB}$, where Z_{LSED} refers to reading from LSED-sensor and Z_{SEB} refers to reading from SEB.

The result has showed that as the mass water content increased from 0% to 120%, the LSED-sensor accuracy is stable, with only 2 mm absolute error comparing to the SEB (Figure B1). As the water content increase further (within a thin layer of water present), the absolute error starts to increase. When the water layer reaches to 1.5 cm, the error is larger than 2 mm as Z_{LSED} decreased significantly.

We conclude that when there is no water or a thin layer water (<1.5 cm) exists on top of the sediment bed, the LSED-sensor can provide reliable bed level data. Thus, LSED-sensors can function well during low tide when the water is drained but could not obtain useful data during high tide or when there is lingering water.

Appendix C: Development of the Machine Learning Predictors for Bed Level Changes

The machine learning predictors built in the present study are based on Artificial Neural Networks (ANN). Prior to the development of these predictors, a pairwise comparison analysis was conducted to reveal the groups of independent variables that are suitable for machine learning applications (Table C1).

Table C1
Pairwise Correlation Analysis of Machine Learning Input Variables

R value	Water depth (h)	H_s	τ_w	τ_c	τ_{mean}	τ_{max}	D_{50}	U_{bottom}	Vegetation density (VD)
Water depth (h)	1	0.66	0.31	0.0006	0.1	0.23	0.08	-0.25	-0.07
H_s		1	0.82	0.39	0.55	0.73	0.18	-0.54	-0.17
τ_w			1	0.61	0.77	0.92	0.55	-0.68	-0.53
τ_c				1	0.96	0.76	0.30	-0.54	-0.34
τ_{mean}					1	0.89	0.37	-0.64	-0.43
τ_{max}						1	0.45	-0.72	-0.54
D_{50}							1	-0.35	-0.92
U_{bottom}								1	0.42
Vegetation density (VD)									1

Each predictor consists of three layers: input layer, hidden layer, and output layer (Figure D1). Before training the model, all the input and output variables were scaled to $[-1, 1]$ using a function called mapminmax (x). Its algorithm is

$$X = \begin{bmatrix} 2 \frac{(\tau_{max} - \min(\tau_{max}))}{(\max(\tau_{max}) - \min(\tau_{max}))} - 1 \\ 2 \frac{(wdp - \min(wdp))}{(\max(wdp) - \min(wdp))} - 1 \\ 2 \frac{(vd - \min(vd))}{(\max(vd) - \min(vd))} - 1 \end{bmatrix}, \quad (C1)$$

$$n = f_1(a[X] + b). \quad (C2)$$

n refers to neurons connected to the input variables by weights (a) and bias (b). f_1 is the transfer function:

$$f_1(n) = \frac{2}{1 + e^{-2n}} - 1, \quad (C3)$$

performing a nonlinear relationship of n . The biases and connection weights are evaluated with a back-propagation algorithm (Levenberg-Marquardt).

$$Z_A = f_2(c \times n + d) \quad (C4)$$

Z_A refers to accumulative bed level changes, whereas c and d connect the neurons to the output Z_A . f_2 (purelin), which is a simple linear function, transferring the neurons in the hidden layer to the output layer.

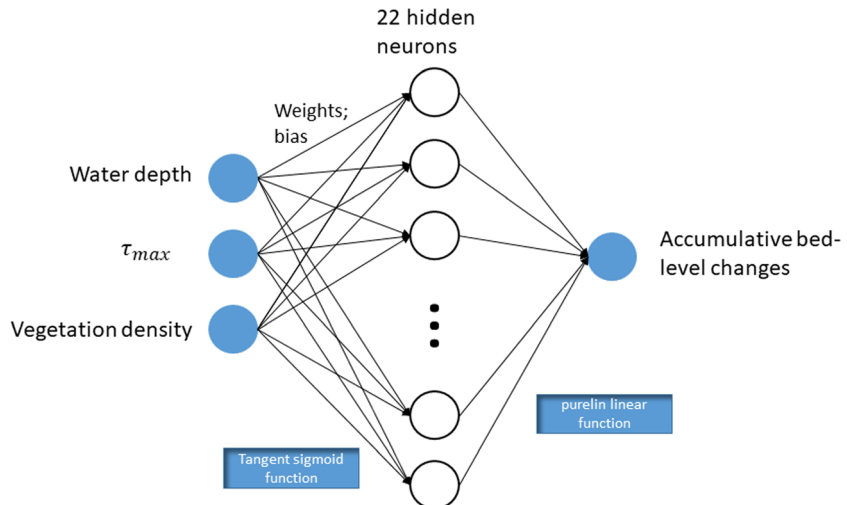


Figure C1. Structure of the machine learning predictor MLP1.

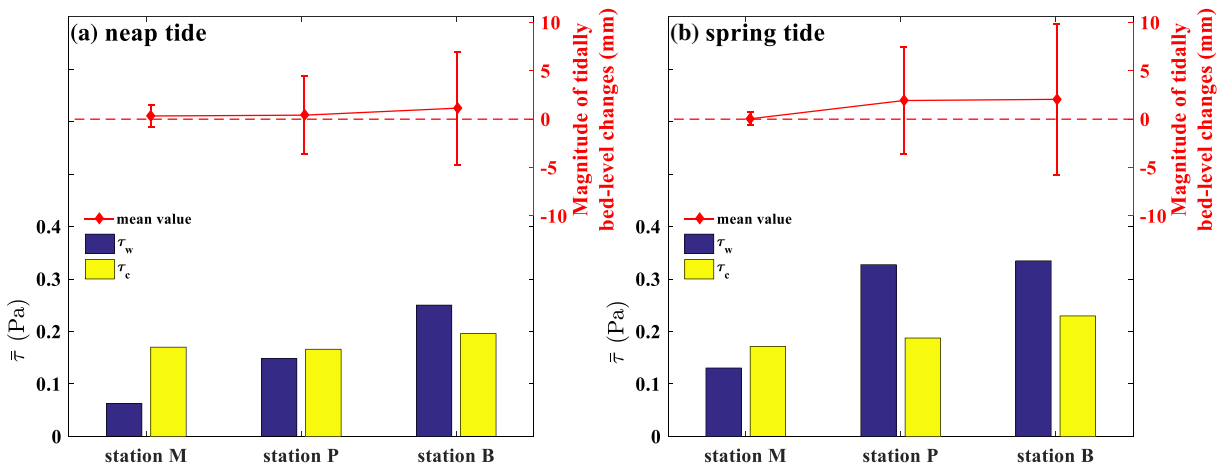


Figure D1. Spatial variation of the magnitude of Z_{tide} and bed shear stress during neap tide. (a) and spring tide. (b) The error bars indicate the standard deviation of the Z_{tide} magnitude due to temporal variation.

The whole data set was randomly divided into three parts: 70% for training set, 15% for validation set, and 15% for testing set. The full data set as well as the weights, biases, and architecture for MLPs will be available online (at <https://zenodo.org/>). To select the optimal number of neurons of the hidden layer, we changed the number of neurons from 1 to 200 to obtain the highest R^2 value with the observation data. For example, 22 hidden neurons were chosen for MLP1 when the R^2 reached up to 0.93 (Figure C1).

Appendix D: Spatial Variation of Z_{tide} Magnitude and Bed Shear Stresses

The spatial distribution of Z_{tide} further shows that the magnitude of bed level change generally decreases from the bare flat toward the mangroves in both neap and spring tides (Figure D1). Spatially, both τ_c and τ_w reduce in the landward direction. At all the stations, the τ_w and τ_w are comparable to each other, except that τ_c is much larger than τ_w at Station M during neap tide. The relative strength between τ_c and τ_w varies between spring and neap tide. During the spring tide, the τ_w is sufficiently increased comparing to the neap tide. However, the variation in τ_c between spring and neap tide conditions is small.

Data Availability Statements

The data, data processing procedure, and machine learning predictors are freely available online (Hu et al., 2020, at 10.4121/uuid:3d971ec0-7a0d-46fa-be02-a2b3d4b9badd).

Acknowledgments

The authors gratefully acknowledge financial supports of the Joint Research Project: NSFC (51761135022), NWO (ALWSD.2016.026), and EPSRC (EP/R024537/1): Sustainable Deltas, a project from National Natural Science Foundation of China (51609269) and Guangdong Provincial Department of Science and Technology (2019ZT08G090).

References

- Andersen, T. J., Pejrup, M., & Nielsen, A. A. (2006). Long-term and high-resolution measurements of bed level changes in a temperate, microtidal coastal lagoon. *Marine Geology*, 226(1–2), 115–125. <https://doi.org/10.1016/j.margeo.2005.09.016>
- Balke, T., Webb, E. L., van den Elzen, E., Galli, D., Herman, P. M. J., & Bouma, T. J. (2013). Seedling establishment in a dynamic sedimentary environment: A conceptual framework using mangroves. *Journal of Applied Ecology*, 50(3), 740–747. <https://doi.org/10.1111/1365-2664.12067>
- Baptist, M. J., Gerkema, T., van Prooijen, B. C., van Maren, D. S., van Regteren, M., Schulz, K., et al. (2019). Beneficial use of dredged sediment to enhance salt marsh development by applying a “Mud Motor”. *Ecological Engineering*, 127, 312–323. <https://doi.org/10.1016/j.ecoleng.2018.11.019>
- Bearman, J. A., Friedrichs, C. T., Jaffe, B. E., & Foxgrover, A. C. (2010). Spatial trends in tidal flat shape and associated environmental parameters in South San Francisco Bay. *Journal of Coastal Research*, 26(2), 342–349.
- Belliard, J.-P., Silinski, A., Meire, D., Kolokythas, G., Levy, Y., van Braeckel, A., et al. (2019). High-resolution bed level changes in relation to tidal and wave forcing on a narrow fringing macrotidal flat: Bridging intra-tidal, daily and seasonal sediment dynamics. *Marine Geology*, 412, 123–138. <https://doi.org/10.1016/j.margeo.2019.03.001>
- Bouma, T. J., van Belzen, J., Balke, T., van Dalen, J., Klaassen, P., Hartog, A. M., et al. (2016). Short-term mudflat dynamics drive long-term cyclic salt marsh dynamics. *Limnology and Oceanography*, 61(6), 2261–2275. <https://doi.org/10.1002/lno.10374>
- Cahoon, D. R., Lynch, J. C., Hensel, P., Boumans, R., Perez, B. C., Segura, B., & Day, J. W. Jr. (2002). High-precision measurements of wetland sediment elevation: I. Recent improvements to the sedimentation-erosion table. *Journal of Sedimentary Research*, 72(5), 730–733. <https://doi.org/10.1306/020702720730>
- Cao, H., Zhu, Z., Balke, T., Zhang, L., & Bouma, T. J. (2018). Effects of sediment disturbance regimes on *Spartina* seedling establishment: Implications for salt marsh creation and restoration. *Limnology and Oceanography*, 63(2), 647–659. <https://doi.org/10.1002/lno.10657>

- Coco, G., Ganthly, F., Sottolichio, A., & Verney, R. (2011). *The use of artificial neural networks to predict intertidal sedimentation and unravel vegetation effects*, (1–9). Beijing, China: River, Coastal and Estuarine Morphodynamics: RCEM 2011.
- Cozzoli, F., Gjoni, V., Del Pasqua, M., Hu, Z., Ysebaert, T., Herman, P. M. J., & Bouma, T. J. (2019). A process based model of cohesive sediment resuspension under bioturbators influence. *The Science of the Total Environment*, 670, 18–30. <https://doi.org/10.1016/j.scitotenv.2019.03.085>
- Dai, Z., Fagherazzi, S., Mei, X., & Gao, J. (2016). Decline in suspended sediment concentration delivered by the Changjiang (Yangtze) River into the East China Sea between 1956 and 2013. *Geomorphology*, 268, 123–132. <https://doi.org/10.1016/j.geomorph.2016.06.009>
- Dai, Z., Mei, X., Darby, S. E., Lou, Y., & Li, W. (2018). Fluvial sediment transfer in the Changjiang (Yangtze) river-estuary depositional system. *Journal of Hydrology*, 566, 719–734. <https://doi.org/10.1016/j.jhydrol.2018.09.019>
- D'Alpaos, A., Toffolon, M., & Camporeale, C. (2016). Ecogeomorphological feedbacks of water fluxes, sediment transport and vegetation dynamics in rivers and estuaries. *Advances in Water Resources*, 93(part B), 151–155. <https://doi.org/10.1016/j.advwatres.2016.05.019>
- Fonstad, M. A., Dietrich, J. T., Courville, B. C., Jensen, J. L., & Carbonneau, P. E. (2013). Topographic structure from motion: A new development in photogrammetric measurement. *Earth Surface Processes and Landforms*, 38(4), 421–430. <https://doi.org/10.1002/esp.3366>
- Friedrichs, C. T. (2011). Tidal flat morphodynamics: A synthesis. In E. Wolanski, & D. McLusky (Eds.), *Treatise on estuarine and coastal science* (pp. 137–170). Waltham: Academic Press. Retrieved from <http://www.sciencedirect.com/science/article/pii/B9780123747112003077>, <https://doi.org/10.1016/B978-0-12-374711-2.00307-7>
- Friedrichs, C. T., & Wright, L. D. (2004). Gravity-driven sediment transport on the continental shelf: Implications for equilibrium profiles near river mouths. *Coastal Engineering*, 51(8–9), 795–811. <https://doi.org/10.1016/j.coastaleng.2004.07.010>
- Gabet, E. J. (1998). Lateral migration and bank erosion in a saltmarsh tidal channel in San Francisco Bay, California. *Estuaries*, 21(4), 745–753. <https://doi.org/10.2307/1353278>
- Ge, Z., Dai, Z., Pang, W., Li, S., Wei, W., Mei, X., et al. (2017). LIDAR-based detection of the post-typhoon recovery of a meso-macro-tidal beach in the Beibu Gulf, China. *Marine Geology*, 391, 127–143. <https://doi.org/10.1016/j.margeo.2017.08.008>
- Goldstein, E. B., & Coco, G. (2014). A machine learning approach for the prediction of settling velocity. *Water Resources Research*, 50, 3595–3601. <https://doi.org/10.1002/2013WR015116>
- Goldstein, E. B., Coco, G., & Plant, N. G. (2019). A review of machine learning applications to coastal sediment transport and morphodynamics. *Earth-Science Reviews*, 194, 97–108. <https://doi.org/10.1016/j.earscirev.2019.04.022>
- Gong, Z., Jin, C., Zhang, C., Zhou, Z., Zhang, Q., & Li, H. (2017). Temporal and spatial morphological variations along a cross-shore intertidal profile, Jiangsu, China. *Continental Shelf Research*, 144, 1–9. <https://doi.org/10.1016/j.csr.2017.06.009>
- Horstman, E. M., Dohmen-Janssen, C. M., Bouma, T. J., & Hulscher, S. J. M. H. (2015). Tidal-scale flow routing and sedimentation in mangrove forests: Combining field data and numerical modelling. *Geomorphology*, 228, 244–262. <https://doi.org/10.1016/j.geomorph.2014.08.011>
- Hu, Z., Lenting, W., van der Wal, D., & Bouma, T. J. (2015). Continuous monitoring bed-level dynamics on an intertidal flat: Introducing novel, stand-alone high-resolution SED-sensors. *Geomorphology*, 245, 223–230. <https://doi.org/10.1016/j.geomorph.2015.05.027>
- Hu, Z., van der Wal, D., Cai, H., van Belzen, J., & Bouma, T. J. (2018). Dynamic equilibrium behaviour observed on two contrasting tidal flats from daily monitoring of bed-level changes. *Geomorphology*, 311, 114–126. <https://doi.org/10.1016/j.geomorph.2018.03.025>
- Hu, Z., Wang, Z. B., Zitman, T. J., Stive, M. J. F., & Bouma, T. J. (2015). Predicting long-term and short-term tidal flat morphodynamics using a dynamic equilibrium theory. *Journal of Geophysical Research: Earth Surface*, 120, 1803–1823. <https://doi.org/10.1002/2015JF003486>
- Hu, Z., Zhou, J., Wang, C., Wang, H., He, Z., Peng, Y., et al. (2020). *Data presented in the paper: A novel instrument for bed dynamics observation supports: machine learning applications in mangrove biogeomorphic processes*. Centre for Research Data. <https://doi.org/10.4121/uuid:3d971ec0-7a0d-46fa-be02-a2b3d4b9badd>
- Hu, Z., Yao, P., van der Wal, D., & Bouma, T. J. (2017). Patterns and drivers of daily bed-level dynamics on two tidal flats with contrasting wave exposure. *Scientific Reports*, 7(1), 7088. <https://doi.org/10.1038/s41598-017-07515-y>
- Jestin, H., Bassoullet, P., Le Hir, P., L'Yavanc, J., & Degres, Y. (1998). Development of ALTUS, a high frequency acoustic submersible recording altimeter to accurately monitor bed elevation and quantify deposition or erosion of sediments. In IEEE Oceanic Engineering Society. OCEANS'98. Conference proceedings (cat. No.98CH36259) (Vol. 1, pp. 189–194). <https://doi.org/10.1109/OCEANS.1998.725734>
- Kratzert, F., Klotz, D., Brenner, C., Schulz, K., & Herrnegger, M. (2018). Rainfall-runoff modelling using long short-term memory (LSTM) networks. *Hydrol. Earth Syst. Sci*, 22(11), 6005–6022.
- Ladd, C. J. T., Duggan-Edwards, M. F., Bouma, T. J., Pagès, J. F., & Skov, M. W. (2019). Sediment supply explains long-term and large-scale patterns in salt marsh lateral expansion and erosion. *Geophysical Research Letters*, 46, 11,178–11,187. <https://doi.org/10.1029/2019GL083315>
- Lawler, D. M. (1991). A new technique for the automatic monitoring of erosion and deposition rates. *Water Resources Research*, 27(8), 2125–2128. <https://doi.org/10.1029/91WR01191>
- Lawler, D. M. (2008). Advances in the continuous monitoring of erosion and deposition dynamics: Developments and applications of the new PEEP-3T system. *Geomorphology*, 93(1–2), 17–39. <https://doi.org/10.1016/j.geomorph.2006.12.016>
- Le Hir, P., Roberts, W., Cazaillet, O., Christie, M., Bassoullet, P., & Bacher, C. (2000). Characterization of intertidal flat hydrodynamics. *Continental Shelf Research*, 20(12–13), 1433–1459. [https://doi.org/10.1016/s0278-4343\(00\)00031-5](https://doi.org/10.1016/s0278-4343(00)00031-5)
- Lee, S. Y., Hamilton, S., Barbier, E. B., Primavera, J., & Lewis, R. R. (2019). Better restoration policies are needed to conserve mangrove ecosystems. *Nature Ecology & Evolution*, 3(6), 870–872. <https://doi.org/10.1038/s41559-019-0861-y>
- Lee, S. Y., & Khim, J. S. (2017). Hard science is essential to restoring soft-sediment intertidal habitats in burgeoning East Asia. *Chemosphere*, 168, 765–776. <https://doi.org/10.1016/j.chemosphere.2016.10.136>
- Leonardi, N., Camacina, I., Donatelli, C., Ganju, N. K., Plater, A. J., Schuerch, M., & Temmerman, S. (2018). Dynamic interactions between coastal storms and salt marshes: A review. *Geomorphology*, 301, 92–107. <https://doi.org/10.1016/j.geomorph.2017.11.001>
- Liu, C., & Nepf, H. (2016). Sediment deposition within and around a finite patch of model vegetation over a range of channel velocity. *Water Resources Research*, 52, 600–612. <https://doi.org/10.1002/2015WR018249>
- Maan, D. C., Van, P., Wang, Z. B., & De, V. (2015). Do intertidal flats ever reach equilibrium? *Journal of Geophysical Research: Earth Surface*, 120, 2406–2436. <https://doi.org/10.1002/2014JF003311>
- Nagihara, S., Mulligan, K. R., & Xiong, W. (2004). Use of a three-dimensional laser scanner to digitally capture the topography of sand dunes in high spatial resolution. *Earth Surface Processes and Landforms*, 29(3), 391–398. <https://doi.org/10.1002/esp.1026>
- Pape, L., Kuriyama, Y., & Ruessink, B. G. (2010). Models and scales for cross-shore sandbar migration. *Journal of Geophysical Research*, 115, F03043. <https://doi.org/10.1029/2009jf001644>

- Pape, L., Ruessink, B. G., Wiering, M. A., & Turner, I. L. (2007). Recurrent neural network modeling of nearshore sandbar behavior. *Neural Networks*, 20(4), 509–518. <https://doi.org/10.1016/j.neunet.2007.04.007>
- Rogers, K., Saintilan, N., & Woodroffe, C. D. (2014). Surface elevation change and vegetation distribution dynamics in a subtropical coastal wetland: Implications for coastal wetland response to climate change. *Estuarine, Coastal and Shelf Science*, 149, 46–56. <https://doi.org/10.1016/j.ecss.2014.07.009>
- Schuerch, M., Spencer, T., Temmerman, S., Kirwan, M. L., Wolff, C., Lincke, D., et al. (2018). Future response of global coastal wetlands to sea-level rise. *Nature*, 561(7722), 231–234. <https://doi.org/10.1038/s41586-018-0476-5>
- Schwarz, C., Gourgue, O., van Belzen, J., Zhu, Z., Bouma, T. J., van de Koppel, J., et al. (2018). Self-organization of a biogeomorphic landscape controlled by plant life-history traits. *Nature Geoscience*, 11(9), 672–677. <https://doi.org/10.1038/s41561-018-0180-y>
- Shi, B., Cooper, J. R., Li, J., Yang, Y., Yang, S. L., Luo, F., et al. (2019). Hydrodynamics, erosion and accretion of intertidal mudflats in extremely shallow waters. *Journal of Hydrology*, 573, 31–39. <https://doi.org/10.1016/j.jhydrol.2019.03.065>
- Soulsby, R. L. (1995). Bed shear stress due to combined waves and currents. In M. J. F. Stive, et al. (Eds.), *Advances in Coastal Morphodynamics* (pp. 4:20–4:23). The Netherlands: Delft. Delft Hydraulics
- Tinoco, R. O., Goldstein, E. B., & Coco, G. (2015). A data-driven approach to develop physically sound predictors: Application to depth-averaged velocities on flows through submerged arrays of rigid cylinders. *Water Resources Research*, 51, 1247–1263. <https://doi.org/10.1002/2014WR016380>
- Truong, S. H., Uijttewaala, W. S. J., & Stive, M. J. F. (2019). Exchange processes induced by large horizontal coherent structures in floodplain vegetated channels. *Water Resources Research*, 55, 2014–2032. <https://doi.org/10.1029/2018WR022954>
- van Bijsterveldt, C. E. J., van Wesenbeeck, B. K., van der Wal, D., Afiati, N., Pribadi, R., Brown, B., & Bouma, T. J. (2020). How to restore mangroves for greenbelt creation along eroding coasts with abandoned aquaculture ponds. *Estuarine, Coastal and Shelf Science*, 235, 106576. <https://doi.org/10.1016/j.ecss.2019.106576>
- Willemsen, P. W. J. M., Borsje, B. W., Hulscher, S. J. M. H., van der Wal, D., Zhu, Z., Oteman, B., et al. (2018). Quantifying bed level change at the transition of tidal flat and salt marsh: Can we understand the lateral location of the marsh edge? *Journal of Geophysical Research: Earth Surface*, 123, 2509–2524. <https://doi.org/10.1029/2018JF004742>
- Yang, S. L., Li, H., Ysebaert, T., Bouma, T. J., Zhang, W. X., Wang, Y. Y., et al. (2008). Spatial and temporal variations in sediment grain size in tidal wetlands, Yangtze Delta: On the role of physical and biotic controls. *Estuarine, Coastal and Shelf Science*, 77(4), 657–671. <https://doi.org/10.1016/j.ecss.2007.10.024>
- Yoo, J.-W., Lee, Y.-W., Lee, C.-G., & Kim, C.-S. (2013). Effective prediction of biodiversity in tidal flat habitats using an artificial neural network. *Marine Environmental Research*, 83, 1–9. <https://doi.org/10.1016/j.marenvres.2012.10.001>
- Yu, Q., Wang, Y., Shi, B., Wang, Y. P., & Gao, S. (2017). Physical and sedimentary processes on the tidal flat of central Jiangsu Coast, China: Headland induced tidal eddies and benthic fluid mud layers. *Continental Shelf Research*, 133, 26–36. <https://doi.org/10.1016/j.csr.2016.12.015>
- Zhao, Y., Yu, Q., Wang, D., Wang, Y. P., Wang, Y., & Gao, S. (2017). Rapid formation of marsh-edge cliffs, Jiangsu coast, China. *Marine Geology*, 385, 260–273. <https://doi.org/10.1016/j.margeo.2017.02.001>
- Zhou, Z., Coco, G., Jiménez, M., Olabarrieta, M., Van Der Wegen, M., & Townend, I. (2014). Morphodynamics of river-influenced back-barrier tidal basins: The role of landscape and hydrodynamic settings. *Water Resources Research*, 50, 9514–9535. <https://doi.org/10.1002/2014WR015891>
- Zhou, Z., Coco, G., Townend, I., Olabarrieta, M., van der Wegen, M., Gong, Z., et al. (2017). Is “morphodynamic equilibrium” an oxymoron? *Earth-Science Reviews*, 165, 257–267. <https://doi.org/10.1016/j.earscirev.2016.12.002>
- Zhou, Z., van der Wegen, M., Jagers, B., & Coco, G. (2016). Modelling the role of self-weight consolidation on the morphodynamics of accretional mudflats. *Environmental Modelling and Software*, 76, 167–181. <https://doi.org/10.1016/j.envsoft.2015.11.002>
- Zhu, Q., van Prooijen, B. C., Wang, Z. B., & Yang, S. L. (2017). Bed-level changes on intertidal wetland in response to waves and tides: A case study from the Yangtze River Delta. *Marine Geology*, 385, 160–172. <https://doi.org/10.1016/j.margeo.2017.01.003>
- Zhu, Q., Yang, S., & Ma, Y. (2014). Intra-tidal sedimentary processes associated with combined wave-current action on an exposed, erosional mudflat, southeastern Yangtze River Delta, China. *Marine Geology*, 347, 95–106. <https://doi.org/10.1016/j.margeo.2013.11.005>
- Zhu, X., Hou, Y., Weng, Q., & Chen, L. (2019). Integrating UAV optical imagery and LiDAR data for assessing the spatial relationship between mangrove and inundation across a subtropical estuarine wetland. *ISPRS Journal of Photogrammetry and Remote Sensing*, 149, 146–156. <https://doi.org/10.1016/j.isprsjprs.2019.01.021>